Chemical Science

Cite this: *Chem. Sci.*, 2012, **3**, 3286

www.rsc.org/chemicalscience

EDGE ARTICLE

The electronic structure and chemical bonding in gold dihydride: AuH_2^- and AuH_2

Hong-Tao Liu,[a] Yi-Lei Wang,[b] Xiao-Gen Xiong,[b] Phuong Diem Dau,[a] Zachary A. Piazza,[a] Dao-Ling Huang,[a] Cong-Qiao Xu,[b] Jun Li*[b] and Lai-Sheng Wang*[a]

Received 17th July 2012, Accepted 14th August 2012
DOI: 10.1039/c2sc20984e

We report an investigation of the electronic structure and chemical bonding of AuH_2^- using photoelectron spectroscopy and *ab initio* calculations. We obtained vibrationally resolved photoelectron spectra of AuH_2^- at several photon energies. Six electronic states of AuH_2 were observed and assigned according to the theoretical calculations. The ground state of AuH_2^- is known to be linear, while that of neutral AuH_2 is bent with a $\angle$H–Au–H equilibrium bond angle of 129°. This large geometry change results in a very broad bending vibrational progression in the photoelectron spectra for the ground-state transition. The electron affinity of AuH_2 is measured to be 3.030 ± 0.020 eV. A short bending vibrational progression is also observed in the second photodetachment band, suggesting a slightly bent structure for the first excited state of AuH_2. The linear geometry is a saddle point for the ground and first excited states of AuH_2, resulting in double-well potentials for these states along the bending coordinate. Spectroscopic evidence is observed for the detachment transitions to the double-well potentials of the ground and first excited states of AuH_2. Higher excited states of AuH_2 due to detachment from the nonbonding Au 5d electrons are all linear, similar to the anion ground state. Kohn–Sham molecular orbital analyses reveal surprising participation of H 2p orbitals in the Au–H chemical bonding and an unprecedented weak Au 5dπ to H 2pπ back donation. The simplicity of the linear AuH_2^- anion and its novel spectroscopic features make it a textbook example for understanding the covalent bonding properties and relativistic effects of Au.

1. Introduction

The chemistry of gold has attracted considerable attention recently due to its importance in homogeneous and heterogeneous catalysis.[1] Among many catalytic reactions, gold hydride is believed to be a key intermediate.[2] However, relatively little is known about gold hydride compounds due to the difficulty in preparing these species.[3] The chemical bonding and electronic structure of the diatomic gold hydride (AuH) have been investigated in a number of experimental studies.[4] The diatomic AuH is an ideal molecule to examine the relativistic effects of gold and has been extensively studied theoretically.[5] However, gold dihydride (AuH_2) is relatively less known. The only experimental observation of AuH_2 and its anion was from an infrared spectroscopy study in a low-temperature H_2 matrix.[6] Theoretical calculations[6,7] suggest that AuH_2^- is thermodynamically stable with a symmetric linear structure, whereas neutral AuH_2 is metastable (relative to Au + H_2) with a bent C_{2v} structure. However, a large potential barrier exists, preventing dissociation of AuH_2 to Au + H_2.[6b,7a–c] On the other hand, the presence of a high reaction barrier also makes the formation of AuH_2 from Au and H_2 very difficult. The reaction of Au^+ with H_2 to form AuH^+ + H was investigated previously.[8] Plasma reactions of Au with a H_2-contianing carrier gas produced only monohydride Au_xH^- species, but not AuH_2^- or any other dihydride species.[4d,e,9] The AuH_2^- anion was only observed in the gas phase recently as a by-product during a multistage mass spectrometry experiment to examine the synthesis and reactivity of dimethylaurate $[CH_3AuCH_3]^-$.[10] However, there have been no experimental spectroscopic studies on gaseous AuH_2^- and AuH_2.

In the current article, we report a joint experimental and theoretical study on the electronic structure and chemical bonding in AuH_2^- and AuH_2. We produced the AuH_2^- anion serendipitously during studies of gold–thiolate complexes using electrospray ionization of a mixed chloro(triphenylphosphine) gold(I) (PPh_3AuCl) and sodium methyl thiolate ($NaSCH_3$) solution in acetonitrile. Vibrationally resolved photoelectron spectra of AuH_2^- have been obtained at various photon energies, yielding a wealth of spectroscopic and electronic information. The photoelectron spectra are interpreted by comparing with high-level *ab initio* calculations. The linear-to-bent structural

[a]*Department of Chemistry, Brown University, Providence, RI 02912, USA. E-mail: lai-sheng_wang@brown.edu*
[b]*Department of Chemistry & Key Laboratory of Organic Optoelectronics and Molecular Engineering of Ministry of Education, Tsinghua University, Beijing 100084, China. E-mail: junli@mail.tsinghua.edu.cn*

transition from the ground state of AuH_2^- to that of AuH_2 gives rise to interesting vibrational features. Molecular orbital analyses reveal for the first time that the H 2p orbitals participate in the chemical bonding between Au and H in AuH_2^-. The linear AuH_2^- species can be viewed as a simple model system to benchmark theoretical methods and study the chemical bonding of gold.

2. Experimental and theoretical method

2.1. Production of AuH_2^- and photoelectron spectroscopy

The experiment was carried out using our magnetic-bottle photoelectron spectroscopy (PES) apparatus equipped with an electrospray ionization (ESI) source, which was described in detail before.[11a] The only modification for the current study was the shortening of the electron flight tube of the magnetic-bottle photoelectron analyzer from 4 to 2.5 meters. The AuH_2^- anions were formed during the ESI experiment to produce $Au(SCH_3)_2^-$ using a solution of PPh_3AuCl and $NaSCH_3$ (~1 mM) in acetonitrile containing a trace amount of methanol. $NaSCH_3$ reacts with PPh_3AuCl in the solution to form $Au(SCH_3)_2^-$. After electrospray ionization, a radio frequency-only quadrupole device guided the $Au(SCH_3)_2^-$ anions from the ESI source into an ion trap, where the anions were accumulated for about 0.1 s before being pulsed into the extraction zone of a time-of-flight (TOF) mass spectrometer. In our recent PES study of Au–thiolate clusters,[11b] we observed Au^- anions from our ESI source, in addition to $Au_x(SCH_3)_{x+1}^-$ type anions, but no gold hydride anions were observed. The Au^- anions were probably produced due to collision-induced dissociation of $Au(SCH_3)_2^-$ either in the ESI source or in the ion trap and have become a convenient calibrant for our PES experiment, as shown in Fig. 1. To enhance the $Au(SCH_3)_2^-$ ion signals, we purged our ESI source region with a flow of N_2 gas. Under this condition, we observed surprisingly both Au^- and AuH_2^- anions (see inset of Fig. 1), which were likely produced through collision induced dissociation (CID) of $Au(SCH_3)_2^-$. Note that no AuH^- was observed. The minimization of air contamination probably allowed AuH_2^- to survive during ESI. Interestingly, both Au^- and AuH_2^- were also observed recently *via* CID of $[(CH_3CO_2)_4Au]^-$ in an ion trap.[10]

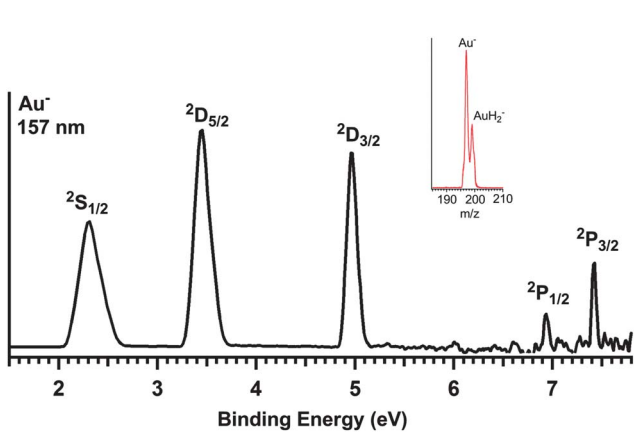

Fig. 1 Photoelectron spectrum of Au^- at 157 nm (7.866 eV). The inset shows the mass spectrum of Au^- and AuH_2^-.

The AuH_2^- anions were selected by a mass gate and decelerated with a momentum decelerator before being photodetached by a laser beam in the interaction zone of the magnetic-bottle photoelectron analyzer. Five different laser wavelengths were used in the current PES experiment. An F_2 excimer laser (157 nm, 7.866 eV) was used to probe a wide binding energy range. To enhance spectral resolution, we performed PES experiments at four lower photon energies: 206 nm (6.013 eV), 245 nm (5.061 eV), 285 nm (4.350 eV) and 300 nm (4.133 eV) from a dye laser. The PES spectra were calibrated using the known spectra of Au^- and I^-.[12] The electron binding energy spectra reported were obtained by subtracting the kinetic energy spectra from the respective detachment photon energies. The electron kinetic energy resolution of the current magnetic-bottle photoelectron analyzer was about 3%, *i.e.*, 30 meV for 1 eV electrons.

2.2. Computational methods

The theoretical studies were performed using relativistic density functional theory (DFT) and *ab initio* wavefunction theory (WFT). DFT calculations were done on AuH_2^- and AuH_2 using the generalized gradient approximation (GGA) with the PBE exchange-correlation functional[13] implemented in the Amsterdam Density Functional program (ADF 2010.01).[14] The Slater basis sets with the quality of triple-ζ plus two polarization functions (TZ2P) were used with the frozen core approximation applied to inner shells [$1s^2$–$4f^{14}$] for Au. The scalar relativistic (SR) and spin–orbit (SO) coupling effects were taken into account by the zero-order-regular approximation (ZORA).[15] Geometries were fully optimized at the SR-ZORA level and single-point energy calculations were performed with inclusion of the SO effects. Vibrational frequency calculations were carried out at the SR-ZORA level to verify that the anion species were true minima. We also did hybrid DFT calculations with B3LYP functional[16] using Gaussian 09.[17] The aug-cc-pVTZ-PP basis sets (11s10p9d3f2g)/[6s6p5d3f2g] for Au and aug-cc-pVTZ basis sets for H (denoted as AVTZ hereafter) were used.[18]

To compare with the experimental PES spectra, we further performed high-level *ab initio* WFT calculations for AuH_2^- using more sophisticated electron correlation methods implemented in the MOLPRO 2008 program.[19] In these calculations, we used both the UCCSD(T) (unrestricted coupled-cluster with single, double and perturbative triple excitations)[20] and CASSCF (complete-active-space self-consistent field) methods.[21] The Stuttgart scalar-relativistic effective core potential (ECP60MDF) was employed for Au,[18a,b] where the 19 valence electrons were treated variationally. We also used the basis sets aug-cc-pVXZ-PP for Au and aug-cc-pVXZ for H (X = D, T, Q)[18b,c] to calculate the vertical detachment energies (VDEs) for comparison of basis set effects. The geometries were optimized at the level of CCSD(T). The electron binding energies corresponding to one-electron transitions from the closed-shell ground state of AuH_2^- to the ground and excited states of AuH_2 were obtained using the CASSCF/CCSD(T)/SO approach that we used previously for $Au(CN)_2^-$, AuI_2^- and $[XAuCN]^-$.[22] In this approach, the SO splittings were treated as a perturbation to the scalar relativistic state energies and were calculated on the basis of CASSCF wave functions with the diagonal matrix elements replaced by the individual CCSD(T) state energies. The SO coupling effect was

included by using a CASSCF state-interacting method[23] with SO pseudopotentials. The CASSCF calculations were performed with 13 electrons in 8 valence orbitals (Au 5d, Au 6s and H 1s), denoted as CASSCF(13e, 8o).

Extensive bonding analyses have been performed to elucidate the interactions between Au and H atoms in AuH_2^-. Natural bond orbital (NBO)[24] and natural resonance theory (NRT)[25] calculations were performed to provide localized bonds and covalent analysis. Wiberg bond orders, natural atomic orbital (NAO) bond indices, and NRT bond orders were also obtained.[24–26]

3. Experimental results

3.1. Photoelectron spectrum of Au^- at 157 nm

Fig. 1 displays the PES spectrum of Au^- measured at 157 nm for comparison with those of the gold dihydride anion. All the spectral features observed in Fig. 1 represent detachment transitions to electronic states of the Au atom. The three peaks at lower binding energies ($^2S_{1/2}$, $^2D_{5/2}$ and $^2D_{3/2}$) are from detachment of a 6s and 5d electron from Au^- ($5d^{10}6s^2$), respectively, and they are usually used to calibrate the conversion from time-of-flight photoelectron data to electron kinetic energies. It is interesting to note that transitions to the $^2P_{1/2}$ and $^2P_{3/2}$ excited states of Au at 6.941 and 7.414 eV are also observed. These two transitions correspond to a final state electron configuration of $5d^{10}6p^1$,[12b] which can only be accessed from the initial state of Au^- ($5d^{10}6s^2$) *via* a two-electron transition or shake-up process, *i.e.*, removal of a 6s electron and excitation of the other 6s electron to the 6p orbital. Such two-electron transitions, due to electron correlation effects, yield the so-called photoelectron satellites and usually exhibit very low cross sections.[27] However, the intensities of the $^2P_{1/2}$ and $^2P_{3/2}$ peaks in Fig. 1 are substantial, suggesting strong electron correlation effects between the two 6s electrons in Au^-. Similarly strong electron correlation effects were observed previously in the PES spectrum of Cu^- at 193 nm.[28]

3.2. Photoelectron spectra of AuH_2^-

Photoelectron spectra of AuH_2^- are shown in Fig. 2 at four different photon energies, 285, 245, 206 and 157 nm. The 157 nm spectrum of AuH_2^- (Fig. 2d) reveals six detachment bands, which are labeled with letters X, A–E. Band X is intense, whereas bands A–E are relatively weak. The spikes around 6 eV and beyond 6.4 eV in the 157 nm spectrum are due to poor signal-to-noise ratios as a result of imperfect background subtraction. At 206 nm (Fig. 2c), the relative intensity of band X is reduced, whereas that of band D is significantly enhanced. Bands B and C are well resolved in the 206 nm spectrum, but their relative intensities are very weak. At 245 nm (Fig. 2b), band A becomes the most intense peak, while the relative intensity of band B is also enhanced. At 285 nm (Fig. 2a), only bands X and A are observed and both are vibrationally resolved. A broad vibrational progression is observed for band X, suggesting a large geometry change between the ground state of AuH_2^- and that of its neutral. Band A is sharp with only a very short vibrational progression and a frequency of 1730 cm^{-1}, as labeled by the vertical lines in Fig. 1a. This should be due to the symmetric

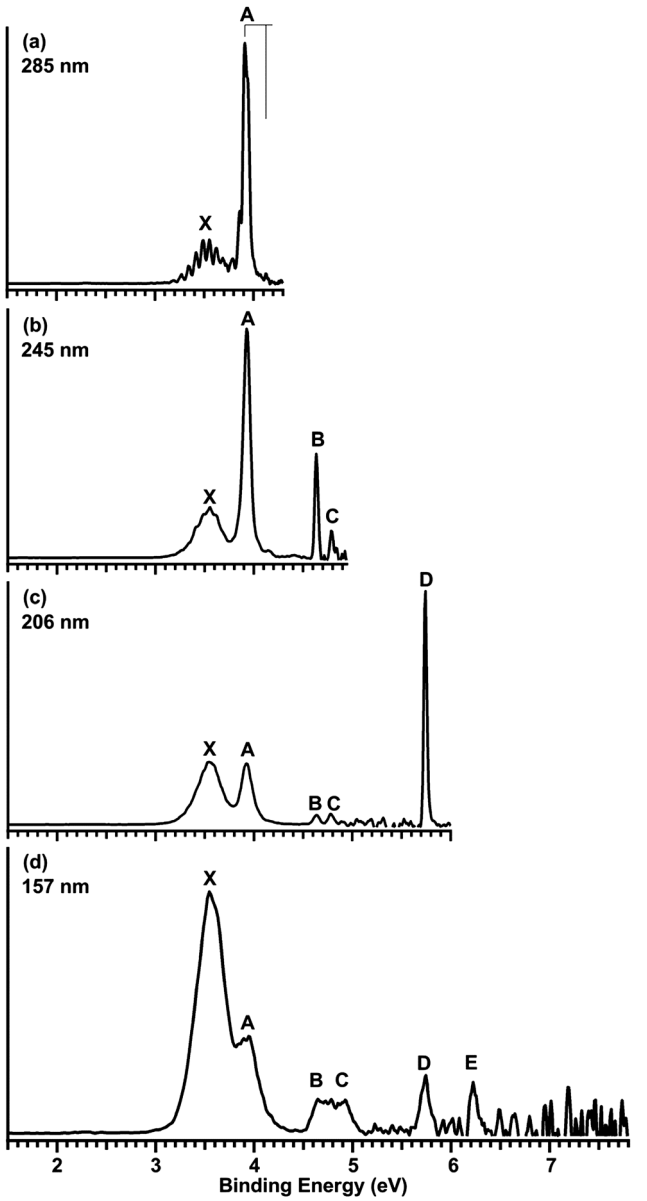

Fig. 2 Photoelectron spectra of AuH_2^- at (a) 285 nm (4.350 eV), (b) 245 nm (5.061 eV), (c) 206 nm (6.013 eV), and (d) 157 nm (7.866 eV). The vertical lines in (a) represent vibrational structures.

Au–H stretching vibrational mode. Bands B, C, D and E are all very sharp without any vibrational structures, suggesting they are derived from non-bonding Au 5d orbitals.

3.3. Analyses of the vibrational structures in bands X and A

Fig. 3 displays a higher resolution spectrum of AuH_2^- at 300 nm. All the peaks are labeled in Fig. 3 and the corresponding binding energies are given in Table 1. A total of eleven vibrational peaks (labeled a–k) are resolved for the ground state band (X). The first ten vibrational peaks form a regular vibrational progression (Table 1, from a–j) and are fitted to the following anharmonic vibrational levels:

$$E_v = (v + 1/2)\omega_h - (v + 1/2)^2\omega_h\chi_e \quad (1)$$

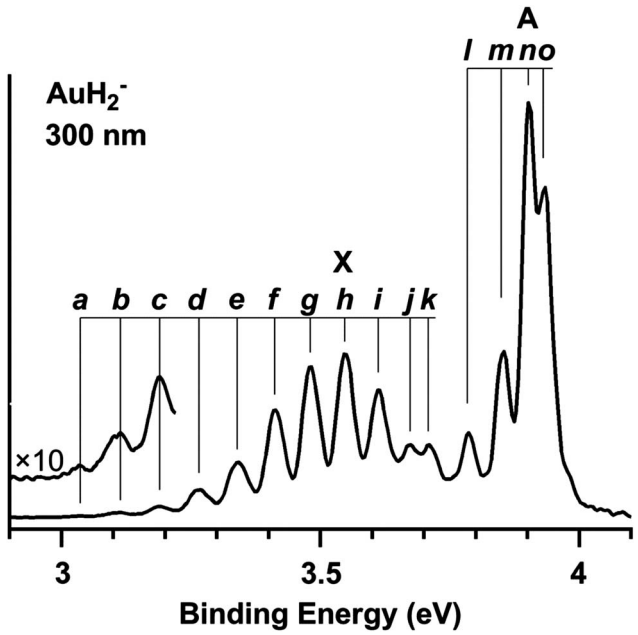

Fig. 3 Photoelectron spectrum of AuH_2^- at 300 nm (4.133 eV); the resolved vibrational structures are labeled with letters and vertical lines. The binding energies of the vibrational peaks are given in Table 1.

Table 1 The energies and spacings of the observed vibrational fine structures for the X and A bands in the 300 nm photoelectron spectrum of AuH_2^- (Fig. 3)

	Peak	Position[a]/eV	Shift[b]/cm^{-1}	Spacing[c]/cm^{-1}
X[d]	a	3.030(20)	0	
	b	3.111(20)	653	653
	c	3.189(20)	1282	629
	d	3.265(20)	1895	613
	e	3.339(20)	2492	597
	f	3.411(20)	3073	581
	g	3.480(20)	3630	557
	h	3.548(20)	4178	548
	i	3.614(20)	4710	532
	j	3.678(20)	5226	516
	k	3.710(20)	5484	258
A[e]	l	3.788(20)	0	
	m	3.852(20)	516	516
	n	3.904(20)	935	419
	o	3.934(20)	977	242

[a] Numbers in parentheses represent the uncertainty in the last digits. [b] Shift relative to the first member of the vibrational progression. [c] Spacing relative to the previous vibrational peak. [d] The harmonic frequency ω_h and the first anharmonic correction $\omega_h\chi_e$ were derived by fitting an anharmonic oscillator to the first ten peaks, a–j: $\omega_h = 670 \pm 20$ cm^{-1} and $\omega_h\chi_e = 9$ cm^{-1}. See text. [e] Another vibrational spacing of 1730 cm^{-1} was observed at 285 nm in Fig. 2a, due to the symmetric stretching mode of AuH_2.

$$\Delta E_v = E_{v+1} - E_v = \omega_h - 2(v+1)\omega_h\chi_e \quad (2)$$

where v is the vibrational quantum number, ω_h is the harmonic frequency, and $\omega_h\chi_e$ is the first anharmonic correction. A harmonic frequency of $\omega_h = 670 \pm 20$ cm^{-1} with an anharmonic correction of $\omega_h\chi_e = 9$ cm^{-1} were obtained. The observed vibrational progression should correspond to the bending vibrational mode of neutral AuH_2 and it exhibits a large anharmonicity of $\chi_e = 0.013$. The fundamental vibrational frequency ($\omega_h - 2\omega_h\chi_e$) of 653 ± 20 cm^{-1} in the gas phase obtained in the current work is in good agreement with the value of 638.1 cm^{-1} measured from the IR spectrum of AuH_2 in a H_2 matrix,[6b] especially when considering the matrix effects that usually reduce the frequencies by 5–20 cm^{-1}. Accordingly, the first observed vibrational peak a is assigned to the 0–0 transition, yielding an ADE of 3.030 ± 0.020 eV for AuH_2^- or the electron affinity (EA) of neutral AuH_2.

However, the spacing between the peaks k and j is 258 cm^{-1} (Table 1), only about half of the spacing between the peaks j and i. For band A, the $v = 1$ peak for the Au–H stretching vibration is not observed in the 300 nm spectrum. However, a short vibrational progression due to the bending mode is resolved, as labeled from l–o (Fig. 3 and Table 1). Interestingly, a similar anomalous vibrational spacing is also observed for band A, which corresponds to detachment transitions to the first excited state of AuH_2. As shown in Fig. 3 and Table 1, the spacing between peaks o and n is 242 cm^{-1}, much smaller than the spacing between m and l (516 cm^{-1}) or that between n and m (419 cm^{-1}). Another surprising observation in band A is the abrupt cutoff of the vibrational progression after peak o. A careful examination also shows that the vibrational progression of band X is abruptly cut off after peak k. As will be shown below, these anomalous vibrational spacings are due to the double-well potentials of the ground and first excited states of AuH_2 because it possesses a bent structure in these states (Fig. 4).

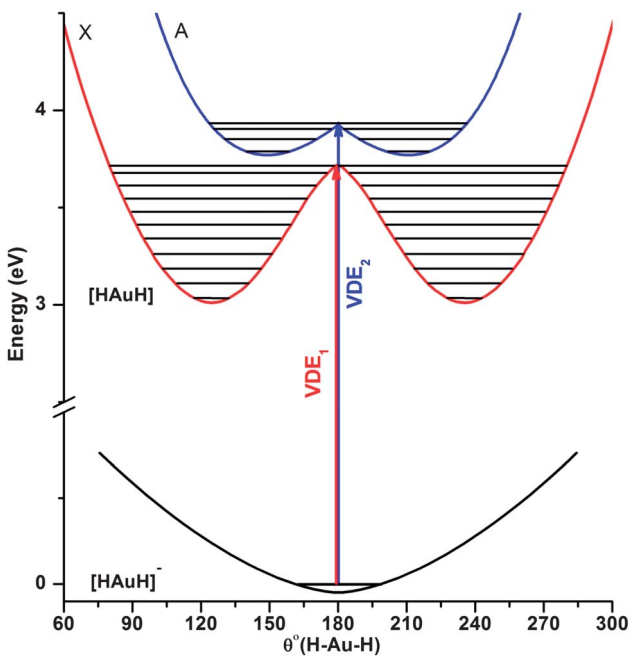

Fig. 4 Schematics showing the double-well potential energy curves along the bending coordinate of the ground state ($^2B_2$) (red) and first excited state ($^2A_1$) (blue) of AuH_2 and the vertical detachment transitions from the ground state ($^1\Sigma_g^+$) (black) of AuH_2^- to the saddle points of the double-well potentials.

Table 2 Observed and calculated vertical (VDE) and adiabatic (ADE) detachment energies for AuH_2^- and the final state assignments. The calculated results are from CCSD(T)/SO calculations with AVQZ basis sets

		VDE/eV		ADE/eV	
	Final state	Expt.[a]	Calc.	Expt.	Calc.
X[b]	$^2\Sigma_{1/2u}$	3.678(20)	3.684	3.030(20)	3.040
A[c]	$^2\Sigma_{1/2g}$	3.904(20)	3.780		
B	$^2\Delta_{5/2g}$	4.635(20)	4.522		
C	$^2\Pi_{3/2g}$	4.785(20)	4.631		
D	$^2\Pi_{1/2g}$	5.745(20)	5.687		
E	$^2\Delta_{3/2g}$	6.22(3)	6.102		

[a] The numbers in parentheses represent the experimental uncertainty in the last digits. [b] See footnote *d* in Table 1. [c] See footnote *e* in Table 1.

The ADEs and VDEs for the observed detachment transitions are given in Table 2, where they are compared with theoretical results as described below.

4. Theoretical results

We have optimized the structure of AuH_2^- and found it to be linear with $D_{\infty h}$ symmetry and a $^1\Sigma_g^+$ ground state. This structure is confirmed to be a minimum through frequency analyses at the DFT level with PBE and B3LYP functionals. The optimized neutral ground state has a bent structure with C_{2v} symmetry at all levels of calculations. The optimized Au–H bond lengths and bond angles of AuH_2^- and AuH_2 at PBE, B3LYP and CCSD(T) are given in Table 3. The structures and bond lengths are consistent with the previous reports.[6,7] Table 3 also includes analyses of the charge distribution and bond orders.

The total energy difference at CCSD(T) level between the anionic and neutral ground states at their respectively optimized geometries gives the ADE, while the total energy difference between the anionic and neutral ground states at the anion geometry gives the first VDE (*i.e.* VDE_1). The higher VDEs were calculated by adding the vertical excitation energies of the neutral molecule calculated at the anion geometry to VDE_1. Table 4 summarizes the calculated VDEs at the CCSD(T) level with three different basis sets, AVDZ, AVTZ and AVQZ. The results of all the three basis sets are consistent, and systematic improvements are observed as the quality of the basis set is increased from AVDZ to AVQZ. The AVQZ results are compared with the experimental data in Table 2.

Table 3 Structural parameters, atomic charges and the calculated bond orders calculated for the ground states of AuH_2 and AuH_2^-

	Method	AuH_2^-	AuH_2
∠H–Au–H/°	CCSD(T)	180	129.23
	PBE	180	129.89
	B3LYP	180	129.38
R(Au–H)/Å	CCSD(T)	1.647	1.595
	PBE	1.664	1.613
	B3LYP	1.665	1.614
Net charge/|e|	Au	−0.0461	0.2303
	H	−0.4770	−0.1151
Bond order	Wiberg	0.5240	0.6228
	NAO	0.5049	0.4055
	NRT	0.4518[a]	0.7139[b]

[a] Covalent 0.2753 (61%), ionic 0.1765 (39%). [b] Covalent 0.4743 (66%), ionic 0.2396 (34%).

Table 4 The VDEs of AuH_2^- calculated with three different basis sets and contributions of SO-free state to SO eigenstates at the AVTZ level

	VDE			
	AVDZ	AVTZ	AVQZ	Contributions of SO-free state to SO eigenstates
X	3.5840	3.6629	3.6836	100% [$^2\Sigma_{1/2u}$]
A	3.6473	3.7284	3.7801	91% [$^2\Sigma_{1/2g}$], 9% [$^2\Pi_{1/2g}$]
B	4.3103	4.4351	4.5224	100% [$^2\Delta_{5/2g}$]
C	4.4190	4.5458	4.6314	77% [$^2\Pi_{3/2g}$], 23% [$^2\Delta_{3/2g}$],
D	5.4850	5.6066	5.6866	88% [$^2\Pi_{1/2g}$], 12% [$^2\Sigma_{1/2g}$],
E	5.8900	6.0159	6.1017	77% [$^2\Delta_{3/2g}$], 23% [$^2\Pi_{3/2g}$]
	7.9927	8.1258	8.1873	97% [$^2\Sigma_{1/2g}$], 3% [$^2\Pi_{1/2g}$]

We also optimized the structures for a number of electronic excited states of AuH_2 at the SR-ZORA level to gain insight into the observed PES spectral features. In contrast to the ground state, we found that all the electronic excited states of AuH_2 are linear with or without SO coupling effects included. However, the first excited state ($^2\Sigma_{1/2g}$) potential energy curve was found to be very flat near ∠H–Au–H = 180° at the DFT level of calculations.

The scalar-relativistic Kohn–Sham MO levels and the SO splittings from the ADF/PBE calculations are shown in Fig. 5 for AuH_2^-. The iso-contour surfaces of the Kohn–Sham orbitals of AuH_2^- calculated using SR-ZORA are displayed in Fig. 6. Contributions to the MOs of AuH_2^- from the Au and H atomic orbitals were analyzed by ADF/PBE/TZ2P calculations, as shown in Table 5. The orbital energy levels of neutral AuH_2 in $D_{\infty h}$ and C_{2v} symmetries are presented in Fig. 7. MO contours of the ground-state neutral AuH_2 based on B3LYP/AVTZ calculations are shown in Fig. 8.

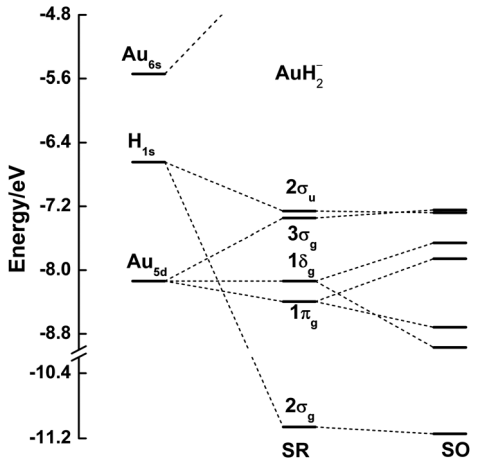

Fig. 5 The orbital energy level correlation diagram for the ground state of AuH_2^- at the scalar relativistic (SR) level with spin–orbit (SO) coupling, where the $2\sigma_u$ is the HOMO. Note that the energy levels of AuH_2^- have been shifted by −6.107 eV to offset the electrostatic shift of the negative charge.

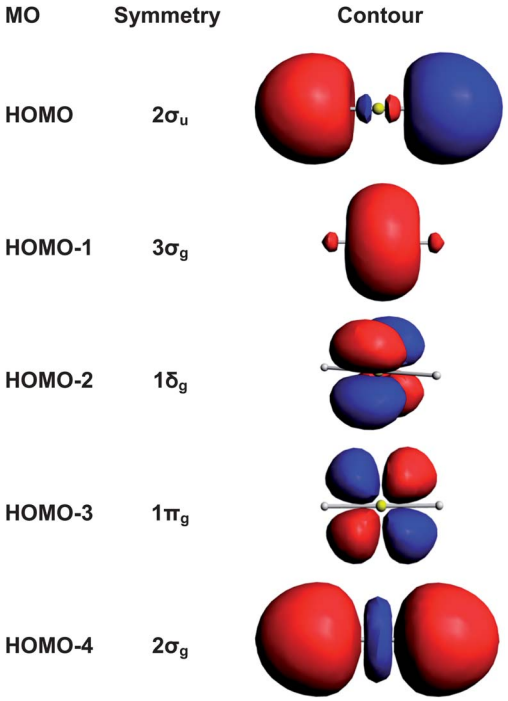

Fig. 6 The contour plots of the occupied valence orbitals of the ground state of AuH_2^- calculated at ADF/PBE/TZ2P level (iso = 0.05 a.u.).

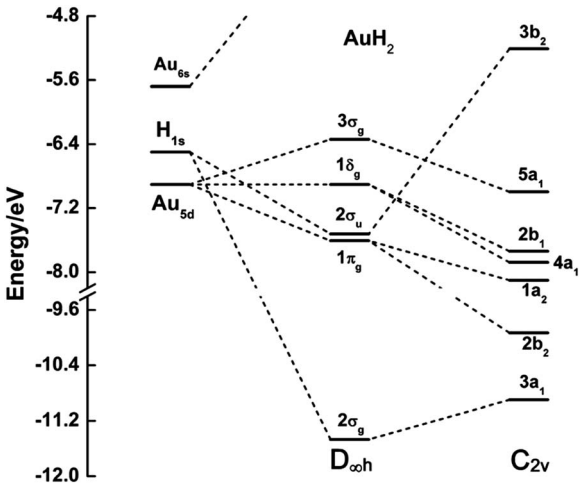

Fig. 7 Orbital energy level correlation diagram for the ground state of AuH_2 in $D_{\infty h}$ and C_{2v} geometries, where the $3\sigma_g$ and $3b_2$ orbitals are singly occupied. The energy of each orbital is drawn on the basis of the RKS single-point calculations. The orbital energies of Au and H are fixed while the energies of AuH_2 are shifted down by about 0.3 eV.

5. Comparison between theoretical and experimental results

The electronic structure of AuH_2^- is fairly simple and can be understood from the orbital interactions between Au and the two H atoms, as shown in Fig. 5 and 6. Bonding interactions between the two H 1s orbitals and Au 6s–5d_{z^2} orbitals lead to the strongly bonding $2\sigma_g$ orbital (1s–5d_{z^2}), the nonbonding or weakly bonding $3\sigma_g$ orbital (6s–5d_{z^2} hybrid), and the nonbonding HOMO $2\sigma_u$ (mainly of antibonding combination of two H 1s orbitals with weak antibonding interactions with Au 6p_z). The $1\delta_g$ and $1\pi_g$ orbitals are nonbonding Au 5d orbitals. The nature of these MOs can be seen in the MO contours in Fig. 6 and quantitatively in Table 5.

5.1. The linear-to-bent transition and the double-well potential of the ground state of AuH_2 (X)

Detachment from the HOMO $2\sigma_u$ gives rise to the X band in the PES spectra of AuH_2^-, corresponding to the ground state of neutral AuH_2. The optimized AuH_2 ground state is the $^2B_2$ state with C_{2v} symmetry with an equilibrium ∠H–Au–H bond angle of 129°, which leads to a double-well potential energy curve for the ground state of neutral AuH_2 with the linear structure as the transition state (Fig. 4). The large bond angle change from the linear AuH_2^- to the bent AuH_2 gives rise to the broad Franck–Condon profile in the bending mode for the X band in the PES spectra of AuH_2^-. The calculated ADE of 3.04 eV is in excellent agreement with the experimental value of 3.030 ± 0.020 eV (Table 2). However, the vertical detachment transition from the linear AuH_2^- leads to AuH_2 in the linear geometry of the $^2\Sigma_{1/2u}$ state, which is a saddle point on the double-well potential curve along the bending coordinate, as schematically shown in Fig. 4. Quantum tunneling will split each vibrational level below the barrier top in each of the double wells,[29] but this tunneling splitting is too small to be resolved in our PES spectra. However, above the barrier top, the tunneling splitting becomes so large that it leads to a reduced vibrational spacing, which is half of that below the barrier top. Therefore, in the ground state of the PES spectra of AuH_2^- (Fig. 3), the peak j is likely near the barrier top and peak k should be above the barrier top, which explains the anomalously small vibrational spacing between peak k and j (Table 1). Consequently, peak j at 3.678 ± 0.020 eV defines the VDE for the ground state transition, *i.e.*, VDE_1. The calculated VDE_1 of 3.684 eV at CCSD(T)/AVQZ/SO is in excellent agreement with the experimental value. Note that, because the vertical transition reaches the saddle point of the double-well potential, one can no longer use the most intense peak h at 3.548 eV (Fig. 3)

Table 5 MO analysis for the ground state of AuH_2^- by ADF/PBE/TZ2P calculations, showing the contributions from Au and H atomic orbitals

MO AuH_2^-	Contribution from Au and H atomic orbitals
HOMO ($2\sigma_u$)	89% H 1s + 11% Au 6p_z
HOMO−1 ($3\sigma_g$)	56% Au 6s + 38% Au 5d_{z^2} + 6% H 1s
HOMO−2 ($1\delta_g$)	100% Au 5d_{xy}, 100% Au 5$d_{x^2-y^2}$
HOMO−3 ($1\pi_g$)	99% Au 5d_{xz} + 1.4% H 2p_x, 99% Au 5d_{yz} + 1.4% H 2p_y
HOMO−4 ($2\sigma_g$)	47% H 1s + 45% Au 5d_{z^2} + 8% Au 6s

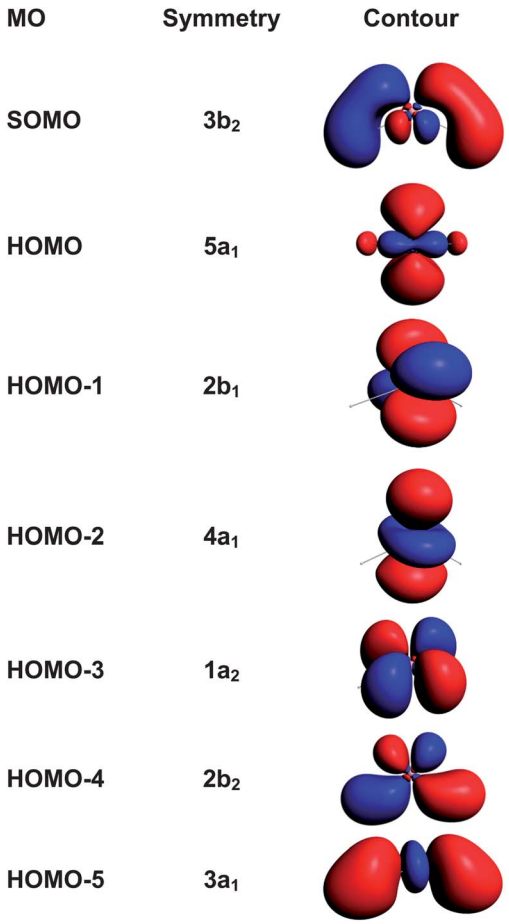

Fig. 8 Molecular orbital contours of neutral AuH_2 calculated at ADF/PBE/TZ2P level (iso = 0.05 a.u.).

as the VDE, as illustrated in Fig. 4 schematically. Furthermore, Franck–Condon factors are expected to be very low or negligible for vibrational levels above the barrier top (see Fig. 4), which explains the apparently abrupt cut-off of the vibrational progression beyond peak k for the X band.

It is interesting to compare the PES spectra of AuH_2^- with that of CuH_2^-.[30] Similar to AuH_2^-, the ground state of CuH_2^- is also linear, whereas the neutral ground state of CuH_2 is bent. However, the equilibrium ∠H–Cu–H bond angle (124°) is even smaller than the ∠H–Au–H bond angle. A very broad and weak PES band was observed for the ground state of CuH_2^-, where the 0–0 transition was not observed, because of the large ∠H–Cu–H bond angle change. An ADE of 2.60 eV was estimated for CuH_2^- from a combination of Franck–Condon simulations and theoretical calculations. This ADE value is reasonable, compared to the 3.030 eV value for AuH_2^-.

5.2. Detachment transition to the slightly bent first excited state of AuH_2 (A)

The HOMO−1 of AuH_2^- is the $3\sigma_g$ orbital (Fig. 5), which is primarily a nonbonding Au 6s–$5d_{z^2}$ hybrid MO with a very weak bonding interaction with the H atoms (Fig. 6 and Table 5). The removal of an electron from the $3\sigma_g$ HOMO−1 results in the A band in the PES spectra, corresponding to the first excited state ($^2\Sigma_{1/2g}$) of AuH_2. Our 285 nm spectrum (Fig. 2a) reveals a vibrational feature with a frequency of 1730 cm^{-1}, which should be due to the symmetric Au–H stretching mode for the first excited state of AuH_2. We note that a similar stretching mode was also observed in the A band of the PES spectrum of CuH_2^- with a frequency of 1880 cm^{-1} for the symmetric Cu–H stretching mode.[30]

However, under the higher resolution condition at 300 nm (Fig. 3), four fine features are resolved for the A band and labeled as l, m, n and o (Table 1). These features should correspond to the bending vibrational mode, suggesting that the first excited state of AuH_2 is slightly bent. Similar to the X band, a double-well behavior is also observed, as schematically shown in Fig. 4. The deviation from linearity is expected to be very small, because the double well can only support two or three bending vibrational levels. In this case, the peak n should be near or below the barrier top and it should define VDE_2 as 3.904 eV. The peak o should be above the barrier top and the abrupt cut-off of the bending vibrational progression is consistent with the double-well potential energy curve. Our calculated VDE_2 is 3.780 eV, which is significantly lower than the experimental value. However, our geometry optimization at the SR-ZORA level predicted a linear geometry for the first excited state of AuH_2, although the potential energy curve is very flat near ∠H–Au–H = 180°. Previous theoretical calculations also predicted that the first excited state of neutral AuH_2 is linear.[6b,7a] Our PES data suggest that the deviation from linearity in the first excited state of AuH_2 is small and the barrier in the double-well potential is very low, as schematically shown in Fig. 4. Because bending favors the $3\sigma_g$ level at the expense of the $2\sigma_u$ level in AuH_2 (see Fig. 7), there is a delicate competition between the bent and linear structures. Clearly, geometry optimization calculations with more sophisticated electron correlation and spin–orbit coupling approach are needed to correctly describe the slightly bent geometry of the first excited state of AuH_2.

5.3. Detachment transitions to higher excited sates of AuH_2 (B–E)

The higher binding energy PES features from B to E are all very sharp without any hint of vibrational excitation, suggesting that they are from detachment of nonbonding orbitals. These features correspond to the second to the fifth electronic excited states of AuH_2, which should all be linear like the ground state of the AuH_2^- anion. Indeed, the HOMO−2 of AuH_2^- is the nonbonding $1\delta_g$ orbital from Au $5d_{xy}$ and $5d_{x^2-y^2}$ (Fig. 6 and Table 5). Detachment from this orbital results in the $^2\Delta_g$ state, which splits to $^2\Delta_{5/2g}$ and $^2\Delta_{3/2g}$ due to SO coupling. The calculated VDEs for these two SO-split states are 4.522 and 6.102 eV, which are in excellent agreement with the observed features B (4.635 eV) and E (6.22 eV), respectively (Table 2). The measured energy splitting between the $^2\Delta_{5/2g}$ and $^2\Delta_{3/2g}$ states in AuH_2 is 1.585 eV, which is only slightly larger than the SO splitting between the $^2D_{5/2}$ and $^2D_{3/2}$ states in the Au atom (1.522 eV), as shown in Fig. 1.

The HOMO−3 of AuH_2^- is the nonbonding $1\pi_g$ orbital from Au $5d_{xz}$ and $5d_{yz}$. Electron detachment from this orbital results in the two SO-split states, $^2\Pi_{3/2g}$ and $^2\Pi_{1/2g}$. The calculated VDEs for these two states are 4.631 and 5.687 eV, which are in good agreement with the observed VDEs for the C (4.785 eV)

and D (5.745 eV) bands, respectively (Table 2). The experimental SO splitting for the $^2\Pi_g$ state is 0.96 eV, which is much smaller than that for the $^2\Delta_g$ state due to the smaller angular momentum of the d_π orbitals than that of the d_δ orbitals. The 206 nm spectrum (Fig. 2c) displays very different relative intensities for bands C and D, even though they are both from detachment of the $1\pi_g$ orbital. This observation can be understood from the different contributions of the SO-free states to the SO eigenstates, as given in Table 4. The C and D states have main contributions from $^2\Pi_{3/2g}$ and $^2\Pi_{1/2g}$ states, respectively, but they have different minor contributions from other SO-free states: the C state contains 23% $^2\Delta_{3/2g}$ state while the D state contains 12% $^2\Sigma_{1/2g}$ (Table 4). The high cross section of the D band should be due to the mixing of the $^2\Sigma_{1/2g}$ state, which has a much higher detachment cross section, as can be seen from the high relative intensity of the A band (91% $^2\Sigma_{1/2g}$) at 285 nm (Fig. 2a) and 245 nm (Fig. 2b). Therefore, spin–orbit coupling not only splits the degenerate states, but also alter the relative intensities of the PES peaks due to the mixing of different SO-free states.

The HOMO−4 is a strong bonding orbital from the H 1s and Au5d_{z^2} orbitals and is mainly responsible for the bonding between Au and H. The covalent interactions of Au–H primarily come from this orbital. Our predicted VDE for this orbital is 8.187 eV (Table 4), which is beyond our photon energy of 7.866 eV at 157 nm.

6. Chemical bonding in AuH_2^- and AuH_2

6.1. Participation of H 2p orbitals in the Au–H bonding in the linear AuH_2^- dihydride

The gold atom in AuH_2^- is formally in its +1 oxidation state, which favors linear coordination with two ligands, such as in the dihalides (AuX_2^-) or dicyanide [$Au(CN)_2^-$]. Recently, we have found significant covalent bonding interactions between Au and the ligands in $Au(CN)_2^-$, AuI_2^-, and their mixed complex $IAuCN^-$.[22] In principle, the bonding in AuH_2^- should be similar to that in the other linear Au(I) complexes, but much stronger covalency is expected between Au and H because they have similar electronegativities and orbital energies. The simplicity of H and its rich spectroscopy features should make AuH_2^- a textbook example to analyze the covalent bonding properties of Au and its spectra.[31] The charge population and bond order analyses of AuH_2^- given in Table 3 reveal that although the H ligands carry most of the negative charge (−0.4770 |e|) the Au atom also carries some slight negative charge, indicating strong covalent interactions between Au–H. The NRT bond analysis shows that AuH_2^- has 61% covalency and a covalent bond order of 0.28.

The chemical bonding in AuH_2^- can be understood from orbital interactions between Au and $H\cdots H^-$. As shown in Fig. 6, the bonding (σ_g) and antibonding (σ_u) MOs of H_2 are still present in the H···Au···H interactions. When Au is inserted between the two H atoms, the bonding orbital is transformed to the strongly bonding $2\sigma_g$ orbital through interactions with the Au $5d_{z^2}$ orbital and the antibonding orbital is transformed into the nonbonding $2\sigma_u$ HOMO in AuH_2^-. It is interesting to note that the HOMO of AuH_2^- is mainly from the antibonding combination of the two H 1s orbitals with a strong contribution from the Au $6p_z$ orbitals (weak antibonding interactions with H 1s), about 11% as shown in Table 5. The HOMO−1 ($3\sigma_g$) of AuH_2^- is primarily an Au 6s–$5d_{z^2}$ nonbonding hybrid, but it contains 6% H 1s (Table 5) and can be considered a weakly bonding orbital between Au and H. The remaining four Au 5d orbitals transform into $1\delta_g$ ($5d_{xy}$, $5d_{x^2-y^2}$) and $1\pi_g$ ($5d_{xz}$, $5d_{yz}$). By symmetry, these orbitals cannot have any interactions with the H 1s orbital and should remain as purely nonbonding in AuH_2^-. However, the $1\pi_g$ orbital is slightly stabilized relative to the $1\delta_g$ orbital (Fig. 5), as revealed by the DFT calculations and the PES experiment. Our MO analysis reveals surprisingly that the $1\pi_g$ orbital contains a 3% contribution from H 2p ($2p_x$ and $2p_y$), which can be considered as a π back-donation from Au 5d to H 2p. This weak π bonding contribution by H stabilizes the $1\pi_g$ orbital relative to the $1\delta_g$ orbital. The back π-bonding from Au 5d to H 2p is unprecedented, which is another beautiful demonstration of the significant relativistic effects of the Au 5d orbitals: The relativistic effects increase the energy of the Au 5d orbitals and expand their radial distributions, making it possible for them to interact with the high-lying H 2p orbitals. All these effects contribute to the strong covalent interactions between Au and H in AuH_2^-. Indeed, the Au–H bond energy ($AuH_2^- \rightarrow AuH + H^-$) is 77 kcal mol^{-1},[22] which is comparable to the Si–H bond strength in SiH_4.[32]

6.2. Chemical bonding in neutral AuH_2

Upon removing an electron from the $2\sigma_u$ HOMO of the linear AuH_2^- anion, the resulting $^2\Sigma_{1/2u}$ neutral ground state is not stable and distorted to a bent structure with a $^2B_2$ electronic state (Fig. 4). This is predicted by the current calculations and all previous theoretical works and confirmed by the extended bending vibrational progression observed in the PES spectra shown in Fig. 2. Our PES spectra suggest that detachment of an electron from the $3\sigma_g$ HOMO−1 also leads to a bent first excited state for AuH_2, albeit the deviation from linearity appears to be very small. However, all previous and the current calculations predict a linear structure, although the current calculations show that the bending potential energy curve for the first excited state of AuH_2 is very flat near $\angle$H–Au–H = 180°. Detachment from the 5d nonbonding $1\delta_g$ and $1\pi_g$ orbitals results in linear excited states for AuH_2, as shown by the sharp PES spectral features (Fig. 2) that indicate no geometry changes upon photodetachment. On the basis of the MO iso-contour surfaces shown in Fig. 6, the $2\sigma_u$ HOMO and $3\sigma_g$ HOMO−1 are weakly antibonding and weakly bonding, respectively. Thus, it is surprising that removal of an electron from these MOs results in bending distortions in the neutral final states. These bending distortions for nondegenerate electronic states are probably due to the second-order Renner–Teller effects, as well as strong electron correlation effects. Fig. 7 shows that the $2\sigma_u$ orbital is significantly stabilized in the linear HAuH molecule due to the weakly antibonding nature of this orbital. However, upon bending, the $1\delta_g$ and $1\pi_g$ orbitals are all stabilized because of the enhanced bonding between the 5d orbitals (δ and π) with the H 1s, whereas the $2\sigma_u$ and $2\sigma_g$ orbitals are destabilized because of the reduced interactions between the $5d_{z^2}$ and the H 1s orbitals. Fig. 8 displays all the valence MO pictures of the bent AuH_2 in its ground state ($^2B_2$). Presumably, the enhanced bonding between

the 5dσ/5dπ and the H 1s outweighs the reduced $5d_{z^2}$–H 1s interaction, resulting in the bent structure.

Our calculated geometrical structures for AuH_2 (Table 3) are consistent with previous calculations.[6b,7a] The double-well barrier height estimated from the energy difference between peaks j and a in Fig. 2 is 0.64 eV. This quantity was calculated to be 0.59 eV previously,[7a–c] in good agreement with our experimental measurement. It is interesting to note that the Au–H bond length (1.595 Å) is shortened slightly in neutral AuH_2 than that in the AuH_2^- anion (1.647 Å), as shown in Table 3. The Au–H bonds in AuH_2 have a covalency of 66% and a covalent bond order of 0.47, suggesting a fairly strong Au–H bonding interaction. The oxidation states of Au and H in neutral AuH_2 can be viewed as +2 and −1, respectively. Its chemical bonding can be described by resonant structures, H–Au···H and H···Au–H, as well as through-space interactions between the two H atoms. The calculated charges of 0.230 |e| for Au and −0.115 |e| for H (Table 3) are consistent with this bonding picture. Although neutral AuH_2 is unstable with respect to Au + H_2 by about 20 kcal mol^{-1},[6b,7a–c] there is a large kinetic barrier for the dissociation. Because of this large barrier, AuH_2^- and AuH_2 cannot be produced by reactions of Au and H_2. The observation of neutral AuH_2 in H_2 matrix was suggested to be from reactions of excited Au* atoms with H_2,[6a] whereas in the current experiment AuH_2^- is formed *via* CID of $Au(SCH_3)_2^-$. The metastability of AuH_2 is consistent with the fact that Au does not have a stable oxidation state of Au(II).

7. Conclusions

We have observed AuH_2^- *via* collision-induced dissociation in an electrospray ionization source and obtained its photoelectron spectra at various photon energies. Extensive vibrational structures are observed for the ground state transition due to the linear to bent structural change between the anion and the neutral. A short bending vibrational progression is also observed for the second PES band, suggesting the first excited state of AuH_2 is slightly bent. Spectroscopic evidence is observed for the double-well bending potential energy curves for the ground and first excited states of AuH_2. Relativistic quantum chemical calculations have been performed to help interpret the experimental data and elucidate the electronic structure and chemical bonding in AuH_2^- and AuH_2. CCSD(T) calculations including spin-orbit effects allow quantitative interpretation of the observed PES features. Strong covalent bonding between Au and H is found. In particular, surprising participation of H 2p orbitals in the Au–H bonding is observed for the first time. The linear AuH_2^- molecule provides a good model system to understand the covalent capabilities of Au and benchmark its relativistic effects.

Acknowledgements

The experimental work done at Brown University was supported by the National Science Foundation (CHE-1049717). The theoretical work done at Tsinghua University was supported by NKBRSF (2011CB932400) and NSFC (20933003, 11079006, 91026003 and 21101098) of China. The calculations were done using the DeepComp 7000 Supercomputer at the Computer Network Information Center, Chinese Academy of Sciences and the Shanghai Supercomputing Center.

References

1 (*a*) D. J. Gorin, B. D. Sherry and F. D. Toste, *Chem. Rev.*, 2008, **108**, 3351; (*b*) A. S. K. Hashmi, *Gold Bull.*, 2004, **37**, 51; (*c*) A. S. K. Hashmi and M. Rudolph, *Chem. Soc. Rev.*, 2008, **37**, 1766; (*d*) A. Corma and H. Garcia, *Chem. Soc. Rev.*, 2008, **37**, 2096.
2 (*a*) A. S. K. Hashmi, *Angew. Chem., Int. Ed.*, 2005, **44**, 6990; (*b*) H. Ito, T. Saito, T. Miyahara, C. M. Zhong and M. Sawamura, *Organometallics*, 2009, **28**, 4829; (*c*) S. Labouille, A. Escalle-Lewis, Y. Jean, N. Mezailles and P. Le Floch, *Chem.–Eur. J.*, 2011, **17**, 2256.
3 (*a*) H. Lehner, D. Matt, P. S. Pregosin, L. M. Venanzi and A. Albinati, *J. Am. Chem. Soc.*, 1982, **104**, 6825; (*b*) E. Y. Tsui, P. Muller and J. R. Sadighi, *Angew. Chem., Int. Ed.*, 2008, **47**, 8937.
4 (*a*) J. Y. Seto, Z. Morbi, F. Charron, S. K. Lee, P. F. Bernath and R. J. Le Roy, *J. Chem. Phys.*, 1999, **110**, 11756; (*b*) U. Ringstrom, *Nature*, 1963, **198**, 981; (*c*) X. F. Wang and L. Andrews, *J. Phys. Chem. A*, 2002, **106**, 3744; (*d*) D. Fischer, A. Wanda, A. Curioni, H. Gronbeck, S. Burkart and G. Gantefor, *Chem. Phys. Lett.*, 2002, **361**, 389; (*e*) S. Buckart, G. Gantefor, Y. D. Kim and P. Jena, *J. Am. Chem. Soc.*, 2003, **125**, 14205; (*f*) T. Okabayashi, E. Y. Okabayashi, M. Tanimoto, T. Furuya and S. Saito, *Chem. Phys. Lett.*, 2006, **422**, 58; (*g*) X. Wu, Z. B. Qin, H. Xie, R. Cong, X. H. Wu, Z. C. Tang and H. J. Fan, *J. Chem. Phys.*, 2010, **133**, 044303.
5 (*a*) G. L. Malli and N. C. Pyper, *Proc. R. Soc. London, Ser. A*, 1986, **407**, 377; (*b*) P. Pyykkö, *Angew. Chem., Int. Ed.*, 2004, **43**, 4412; (*c*) P. Pyykkö, *Chem. Soc. Rev.*, 2008, **37**, 1967; (*d*) P. Pyykkö, *Inorg. Chim. Acta*, 2005, **358**, 4113; (*e*) H. A. Witek, T. Nakijima and K. Hirao, *J. Chem. Phys.*, 2000, **113**, 8015; (*f*) P. Schwerdtfeger, J. R. Brown, J. K. Laerdahl and H. Stoll, *J. Chem. Phys.*, 2000, **113**, 7110.
6 (*a*) L. Andrews and X. F. Wang, *J. Am. Chem. Soc.*, 2003, **125**, 11751; (*b*) L. Andrews, X. F. Wang, L. Manceron and K. Balasubramanian, *J. Phys. Chem. A*, 2004, **108**, 2936.
7 (*a*) M. Guitou-Guichemerre and G. Chambaud, *J. Chem. Phys.*, 2005, **122**, 204325; (*b*) K. Balasubramanian and M. Z. Liao, *Chem. Phys.*, 1988, **127**, 313; (*c*) K. Balasubramanian and M. Z. Liao, *J. Phys. Chem.*, 1989, **93**, 89; (*d*) P. Schwerdtfeger, P. D. W. Boyd, A. K. Burrell, W. T. Robinson and M. J. Taylor, *Inorg. Chem.*, 1990, **29**, 3593.
8 (*a*) F. X. Li, C. S. Hinton, M. Citir, F. Y. Liu and P. B. Armentrout, *J. Chem. Phys.*, 2011, **134**, 024310; (*b*) A. Dorta-Urra, A. Zanchet, O. Roncero, A. Aguado and P. B. Armentrout, *J. Chem. Phys.*, 2011, **135**, 091102.
9 H. J. Zhai, B. Kiran and L. S. Wang, *J. Chem. Phys.*, 2004, **121**, 8231.
10 N. J. Rijs, G. B. Sanvido, G. N. Khairallah and R. A. J. O'Hair, *Dalton Trans.*, 2010, **39**, 8655.
11 (*a*) L. S. Wang, C. F. Ding, X. B. Wang and S. E. Barlow, *Rev. Sci. Instrum.*, 1999, **70**, 1957; (*b*) C. G. Ning, X. G. Xiong, Y. L. Wang, J. Li and L. S. Wang, *Phys. Chem. Chem. Phys.*, 2012, **14**, 9323.
12 (*a*) J. C. Rienstra-Kiracofe, G. S. Tschumper, H. F. Schaefer III, S. Nandi and G. B. Ellison, *Chem. Rev.*, 2002, **102**, 231; (*b*) C. E. Moore, Atomic Energy Levels, *Natl. Stand. Ref. Data Ser. (U. S. Natl. Bur. Stand.)*, 1971, **2**, 467.
13 J. P. Perdew, K. Burke and M. Ernzerhof, *Phys. Rev. Lett.*, 1996, **77**, 3865.
14 *ADF 2010.01*, http://www.scm.com.
15 E. van Lenthe, R. van Leeuwen, E. J. Baerends and J. G. Snijders, *Int. J. Quantum Chem.*, 1996, **57**, 281.
16 (*a*) A. D. Becke, *J. Chem. Phys.*, 1993, **98**, 5648; (*b*) C. T. Lee, W. T. Yang and R. G. Parr, *Phys. Rev. B*, 1988, **37**, 785.
17 M. J. Frisch, G. W. Trucks, H. B. Schlegel, G. E. Scuseria, M. A. Robb, J. R. Cheeseman, G. Scalmani, V. Barone, B. Mennucci, G. A. Petersson, H. Nakatsuji, M. Caricato, X. Li, H. P. Hratchian, A. F. Izmaylov, J. Bloino, G. Zheng, J. L. Sonnenberg, M. Hada, M. Ehara, K. Toyota, R. Fukuda, J. Hasegawa, M. Ishida, T. Nakajima, Y. Honda, O. Kitao, H. Nakai, T. Vreven, J. A. Montgomery, Jr., J. E. Peralta, F. Ogliaro, M. Bearpark, J. J. Heyd, E. Brothers, K. N. Kudin, V. N. Staroverov, R. Kobayashi, J. Normand, K. Raghavachari, A. Rendell, J. C. Burant, S. S. Iyengar, J. Tomasi, M. Cossi, N. Rega, J. M. Millam, M. Klene, J. E. Knox, J. B. Cross, V. Bakken, C. Adamo, J. Jaramillo, R. Gomperts, R. E. Stratmann, O. Yazyev, A. J. Austin, R. Cammi, C. Pomelli, J. Ochterski, R. L. Martin, K. Morokuma, V. G. Zakrzewski, G. A. Voth, P. Salvador, J. J. Dannenberg, S. Dapprich, A. D. Daniels, O. Farkas,

J. B. Foresman, J. V. Ortiz, J. Cioslowski and D. J. Fox, *GAUSSIAN 09 (Revision A.2)*, Gaussian, Inc., Wallingford, CT, 2009.
18 (*a*) D. Figgen, G. Rauhut, M. Dolg and H. Stoll, *Chem. Phys.*, 2005, **311**, 227; (*b*) K. A. Peterson and C. Puzzarini, *Theor. Chem. Acc.*, 2005, **114**, 283; (*c*) T. H. Dunning, *J. Chem. Phys.*, 1989, **90**, 1007.
19 H. J. Werner, *MOLPRO, version 2008.1*, http://www.molpro.net.
20 (*a*) G. D. Purvis and R. J. Bartlett, *J. Chem. Phys.*, 1982, **76**, 1910; (*b*) G. E. Scuseria, C. L. Janssen and H. F. Schaefer, *J. Chem. Phys.*, 1988, **89**, 7382.
21 B. O. Roos and P. R. Taylor, *Chem. Phys.*, 1980, **48**, 157.
22 (*a*) X. B. Wang, Y. L. Wang, J. Yang, X. P. Xing, J. Li and L. S. Wang, *J. Am. Chem. Soc.*, 2009, **131**, 16368; (*b*) L. Wang, X. B. Wang, X. P. Xing, F. Wei, J. Li and L. S. Wang, *J. Phys. Chem. A*, 2010, **114**, 11244; (*c*) H. T. Liu, X. G. Xiong, P. D. Dau, Y. L. Wang, J. Li and L. S. Wang, *Chem. Sci.*, 2011, **2**, 2101.
23 A. Berning, M. Schweizer, H. J. Werner, P. J. Knowles and P. Palmieri, *Mol. Phys.*, 2000, **98**, 1823.
24 (*a*) J. P. Foster and F. Weinhold, *J. Am. Chem. Soc.*, 1980, **102**, 7211; (*b*) A. E. Reed, R. B. Weinstock and F. Weinhold, *J. Chem. Phys.*, 1985, **83**, 735.
25 E. D. Glendening and F. Weinhold, *J. Comput. Chem.*, 1998, **19**, 593.
26 K. B. Wiberg, *Tetrahedron*, 1968, **24**, 1083.
27 S. Suzer, S. T. Lee and D. A. Shirley, *Phys. Rev. A: At., Mol., Opt. Phys.*, 1976, **13**, 1842.
28 H. B. Wu, S. R. Desai and L. S. Wang, *J. Phys. Chem. A*, 1997, **101**, 2103.
29 (*a*) S. Carniato, *J. Chem. Phys.*, 2007, **126**, 224307; (*b*) C. K. Lin, H. C. Chang and S. H. Lin, *J. Phys. Chem. A*, 2007, **111**, 9347.
30 R. M. D. Calvi, D. H. Andrews and W. C. Lineberger, *Chem. Phys. Lett.*, 2007, **442**, 12.
31 L. S. Wang, *Phys. Chem. Chem. Phys.*, 2010, **12**, 8694.
32 B. Kiran, X. Li, H. J. Zhai, L. F. Cui and L. S. Wang, *Angew. Chem., Int. Ed.*, 2004, **43**, 2125.